# Support Information

# Nano composite of Nb-based binary phase for lowering activation energy of $Li^+$ intercalation as anode of high-performance aqueous dual-ion battery

Dengyao Yang[a]*, Junko Matsuda[a], Jun Tae Song[a,b], Motonori Watanabe[a,b], Tatsumi Ishihara[a,b]*

[a] International Institute for Carbon-Neutral Energy Research (WPI-$I^2$CNER), Kyushu University, Fukuoka 819-0395, Japan

[b] Department of Applied Chemistry, Faculty of engineering, Kyushu University, Fukuoka 819-0395, Japan

## Experimental

### Concentrated aqueous electrolyte preparation

Lithium bis(trifluoromethane sulfonyl) imide ($LiN(SO_2CF_3)_2$, LiTFSI, Kishida Chem. Co. Ltd.) and Lithium bis(fluorosulfonyl) imide ($LiN(SO_2F)_2$, LiFSI, Kishida Chem.Co. Ltd) were used as supporting salts with a molar ratio of LiFSI:LiTFSI=9:1. Hybrid solvent is consisted from distilled water and tetraethylene glycol dimethyl ether (tetraglyme, G4, Fujifilm Wako Pure Chem. Co. Ltd.) with a weight ratio of 8:2. Saturated 9LiFSI/1LiTFSI of 37 mol are dissolved in 1 kg hybrid solvent of $8H_2O$/2G4 to obtain concentrated aqueous electrolyte, named as 37 mol $kg^{-1}$ 9LiFSI/1LiTFSI-$8H_2O$/2G4.[1]

### Electrode preparation

Positive electrode is consisted of KS6 graphite (Imerys Graphite & Carbon), conductive acetylene black (Denki Kagaku Kogyo) and sodium carboxymethylcellulose (CMC, type 1170, Daicel Fine Chem Ltd.) with a weight ratio of 80:15:5. For negative electrode, m-MNO (m equal to Mn, Fe, Ni), conductive acetylene black (Denki Kagaku Kogyo) and polyvinylidene difluoride (PVdF, 8 wt.% NMP solution) with a weight ratio of 80:10:10 was used. Active materials of positive and negative electrodes were used 0.6 mg $cm^{-2}$ and 0.6 mg $cm^{-2}$, respectively. KS6/M-MNO full cell was constructed in Ar atmosphere using a KS6 positive electrode, M-MNO negative electrode and glass fiber separator in a commercial two-electrode cell (SB2A, EC frontier).

### Material Characterization

XRD patterns of synthesized samples were obtained on a high-resolution diffractometer (SmartLab, Rigaku) with Cu Kα radiation (40 kV, 80 mA) in the 2θ range from 10° to 60° at a scan rate of 0.05° $s^{-1}$. For the ex-situ XRD measurements, the Fe-MNO electrodes were measured after charge/discharge to objective potential and disassembled a Fe-MNO/AC half-cell in the 3-electrode test cell or graphite/Fe-MNO dual-ion battery in the 2-electrode test cell. SEM images of prepared samples were

carried out from a scanning electron microscope (FEI, Versa 3D HiVac) at a voltage of 20 kV. XPS spectroscopy was conducted on a high sensitivity photoelectron spectrometer (Kratos Ultra2, Shimazu) with Mg Kα radiation.

**Calculation of energy density for KS6/AC dual-ion battery using 20mol/kg W1A1 electrolyte**

Since dissolved salts in electrolyte is the only source of ions, the energy density is determined by the number of ions in dual-ion battery.[2-4] In addition, discharge voltage also affects energy density in calculation. As shown in text part, KS6/AC dual-ion battery using 37 mol $kg^{-1}$ 9LiFSI-1LiTFSI/8$H_2O$-2G4 electrolyte possesses an average discharge voltage of 2.2 V. Therefore, the gravimetric energy density of constructed KS6/Fe-MNO dual-ion battery using 37 mol $kg^{-1}$ 9LiFSI-1LiTFSI/8$H_2O$-2G4 electrolyte are calculated as reported method. **Equation S1** and **S2** is based on all supporting salts in electrolyte intercalated.[5-7]

$$Q_e = N_A * n_e * e \quad (S1)$$

Here, $\boldsymbol{Q_e}$ is total electric quantity in a cell used electrolyte. $\boldsymbol{N_A}$, Avogadro constant, $6.02*10^{23}$. $\boldsymbol{n_e}$, molar quantity of supporting salts in a cell used electrolyte. **e**, elementary charge, $1.6*10^{-19}$C.

$$u_m = \frac{Q_e * V_a}{m_a + m_c + m_e} \quad (S2)$$

$u_m$ is gravimetric energy density, Wh $kg^{-1}$. $V_a$ is average discharge voltage of KS6/$Mo_6S_8$ dual-ion battery, 2.2 V. $m_a$, $m_c$, and $m_e$ is mass of anode ($1.2*10^{-3}$ g), cathode ($1.2*10^{-3}$ g) and electrolyte (0.67 g) in a KS6/Fe-MNO dual-ion battery. Here, since porous polypropylene (PP) thin film will be used in commercial cell, the mass of pp film may be quite small and so it could be ignored the weight of separator weight when the energy density was calculated.

By calculation, the theoretical energy density of KS6/Fe-MNO dual-ion battery using 37 mol $kg^{-1}$ 9LiFSI-1LiTFSI/8$H_2O$-2G4 electrolyte was estimated to be 250 Wh $kg^{-1}$.

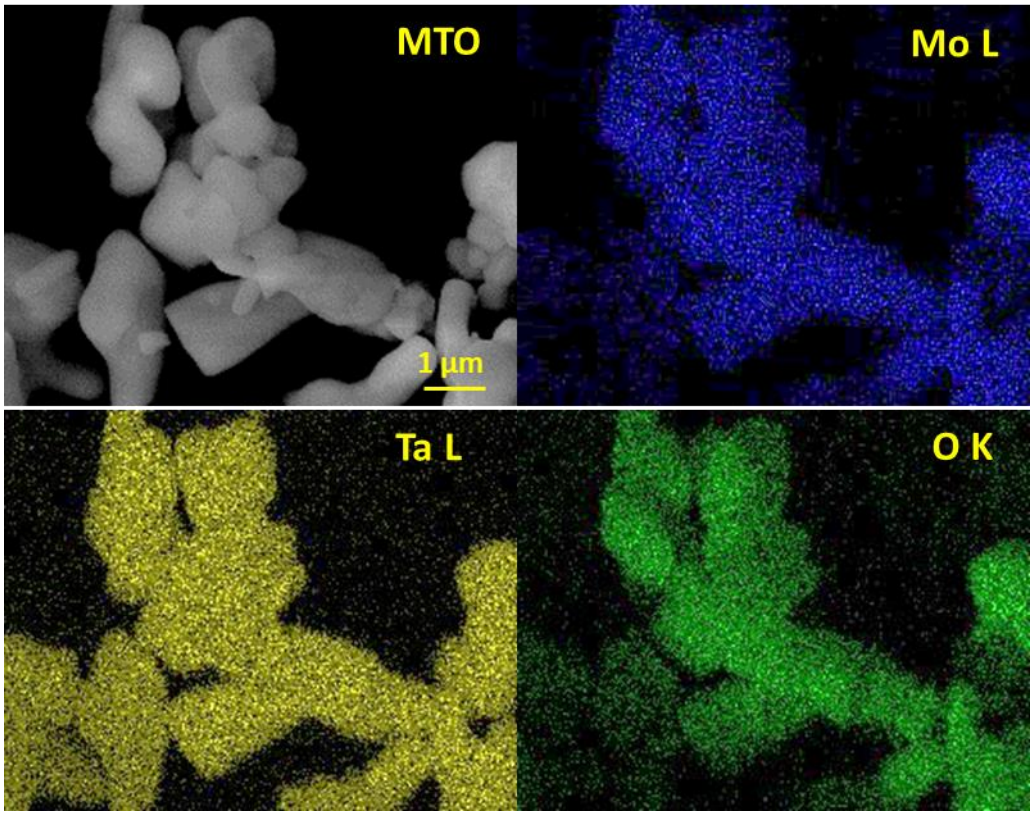


Fig. S1 SEM and EDX mapping images of prepared $MoTa_{12}O_{33}$.

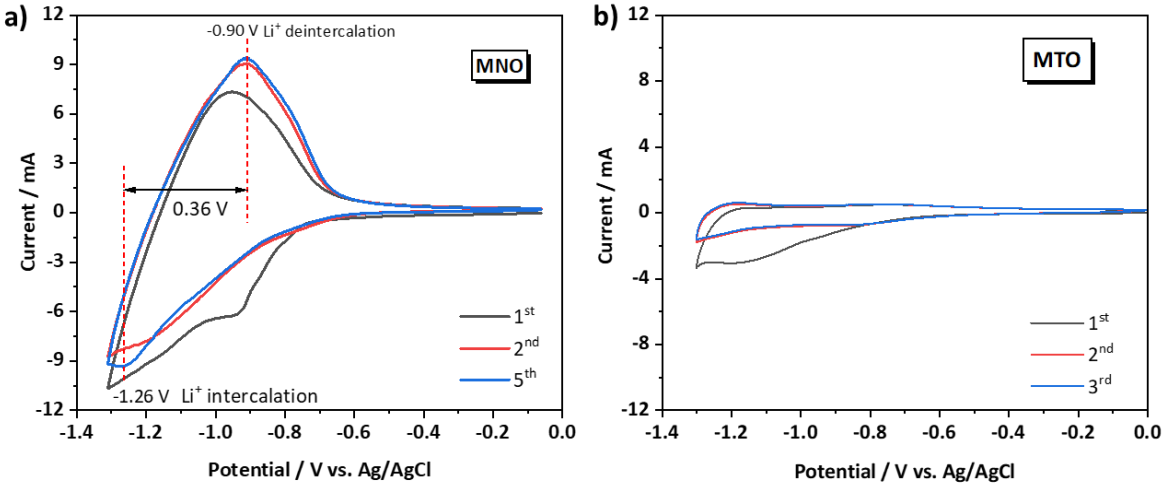


Fig. S2 CV curves of a), MNO and b), MTO in 37 mol $kg^{-1}$ 9LiFSI/1LiTFSI-8$H_2O$/2G4 electrolyte. (Potential range: -1.3~0 V vs. Ag/AgCl; Sweep rate: 5 mV $s^{-1}$; Three electrodes system with an Ag/AgCl reference electrode)

Compared to MNO, MTO performed almost no capacity to $Li^+$ intercalation. Even there are current response in reduction process from the CV curves (Fig. S2b), that can be assigned to electrolyte reduction occurred on surface of electrode. In addition, no oxidation peak is appeared indicates Li extraction reaction absent in oxidation process.

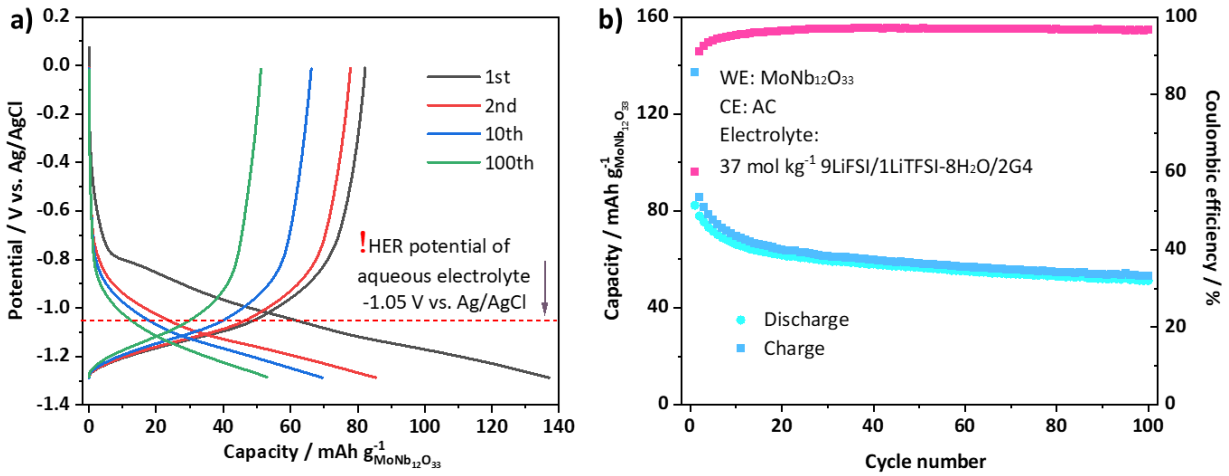


Fig. S3 a) Charge-discharge profiles and b) cycle performance of $MoNb_{12}O_{33}$/AC half-cell using 37 mol $kg^{-1}$ 9LiFSI/1LiTFSI-8$H_2O$/2G4 electrolyte (Potential range: -1.3~0 V vs. Ag/AgCl, Current density: 0.4 mA $cm^{-2}$, Three electrodes system with an Ag/AgCl reference electrode).

The hydrogen evolution reaction potential of applied aqueous electrolyte is -1.05 V vs. Ag/AgCl as we reported in previous work.[1] It is noted that the half-cell of MNO/AC is discharged to -1.3 V vs. Ag/AgCl, which is far higher than the HER potential of electrolyte. However, as shown in the Fig. S3b, the cell showed a quite good coulombic efficiency in the potential range of -1.3 ~ 0 V vs. Ag/AgCl, indicating MNO performed a good anticatalysts of water reduction.

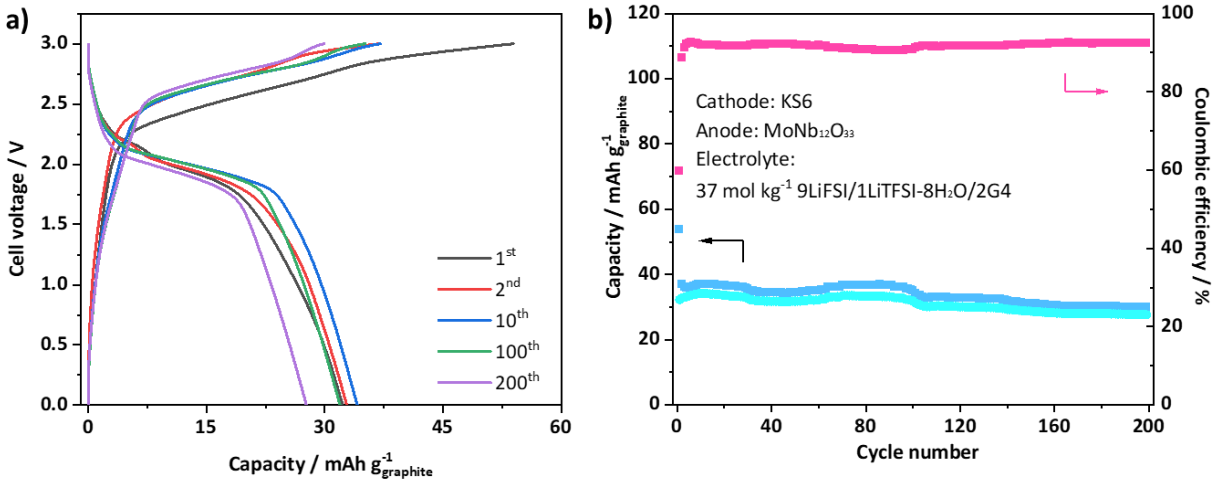


Fig. S4 a) Charge-discharge curves and b) cycle performance of Graphite/$MoNb_{12}O_{33}$ dual-ion battery using 37 mol $kg^{-1}$ 9LiFSI/1LiTFSI-8$H_2O$/2G4 electrolyte. (Voltage range: 0~3 V; Current density: 0.6 mA $cm^{-2}$)

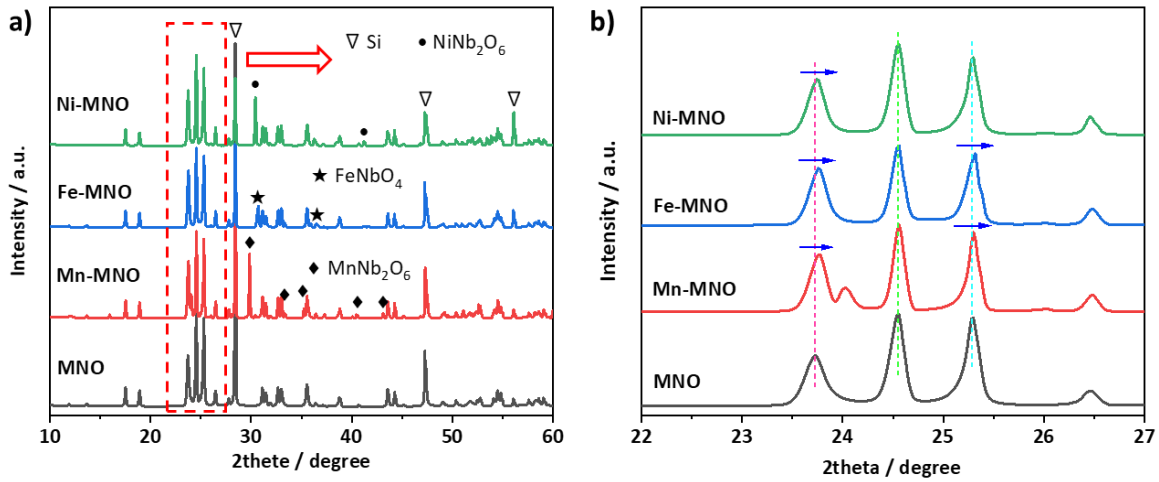


Fig. S5 XRD patterns of synthesized varied niobium-based composite materials.

To eliminate deviation due to measurement, Si powder was mixed to original samples as an internal standard substance. A shown in Fig. S5, the characteristic peak of Si was calibrated to 28.4° that corresponds to (1,1,1) crystal plane.

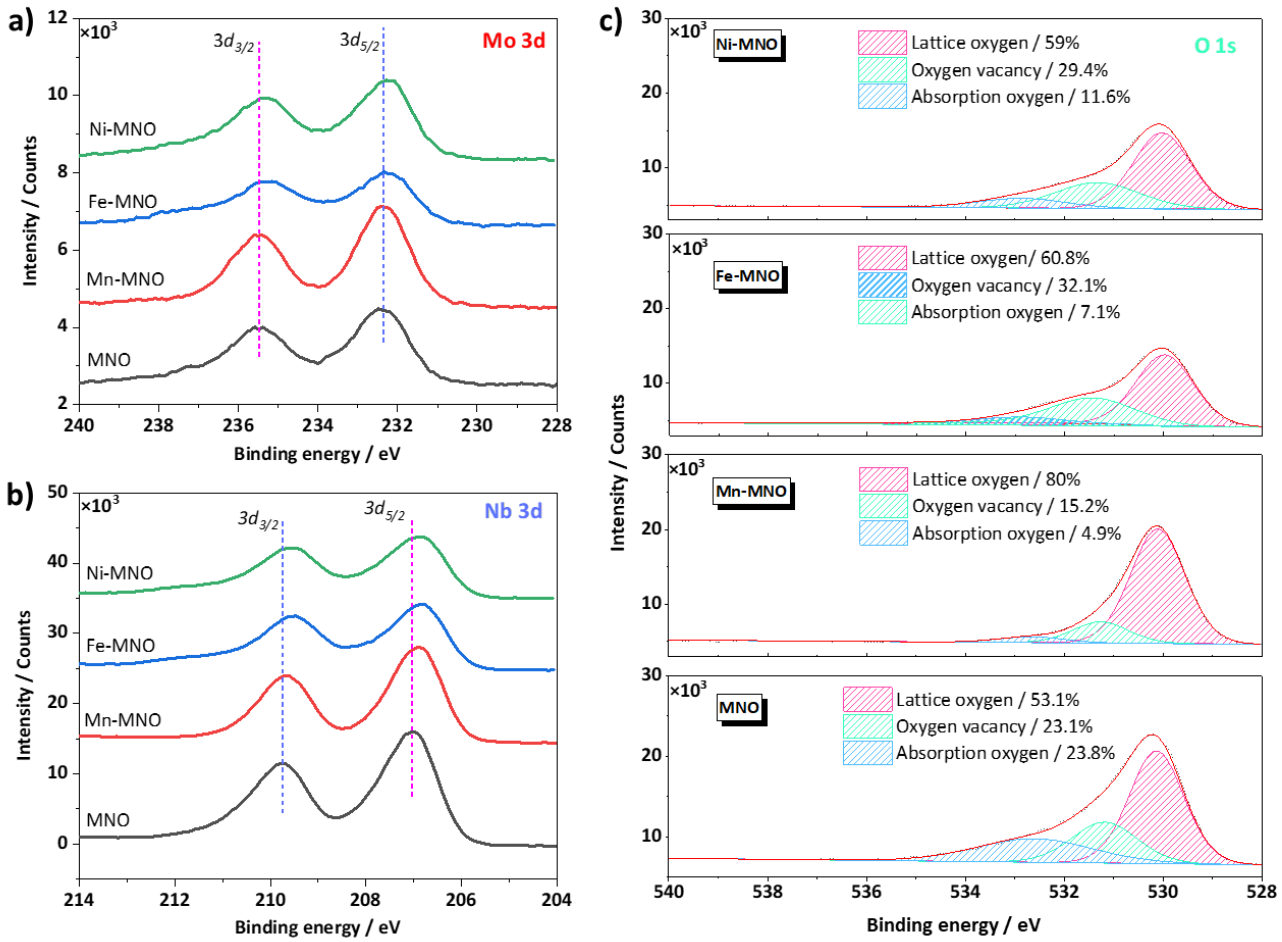


Fig. S6 XPS spectra of synthesized various niobium-based composite materials. a) Mo 3d, b) Nb 3d, c) O 1s XPS peaks.

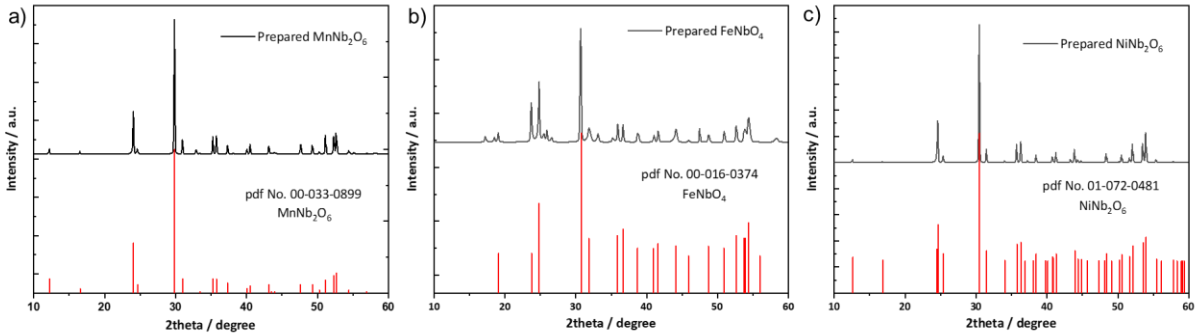


Fig. S7 XRD patterns of prepared niobate. a), $MnNb_2O_6$; b), $FeNbO_4$; c), $NiNb_2O_6$.

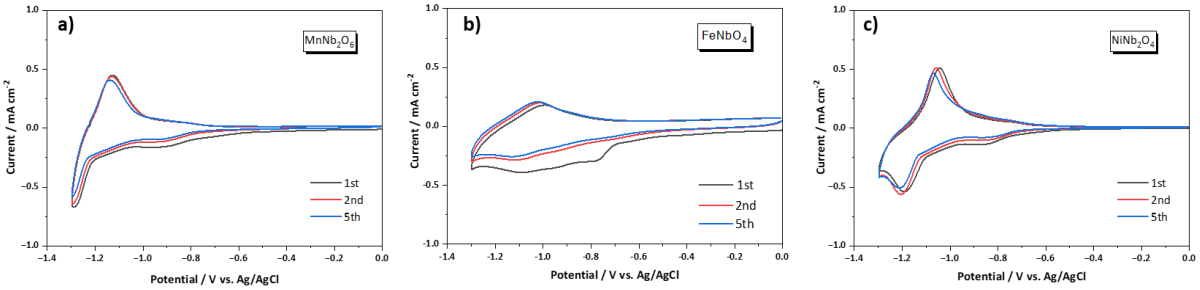


Fig. S8 CV curves of varying prepared Niobate. a) $MnNb_2O_6$, b) $FeNbO_4$, c) $NiNb_2O_6$.

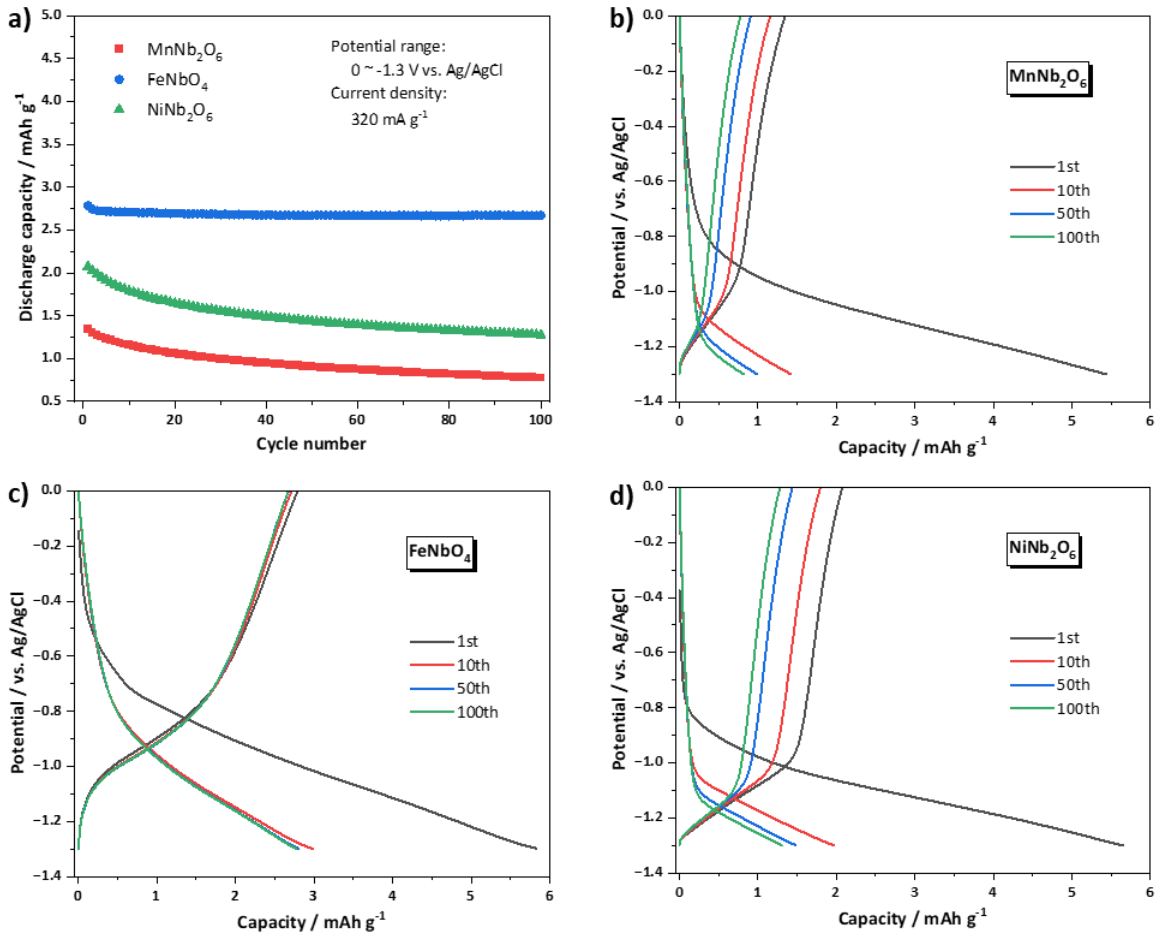


Fig. S9 a) Cycle performance of varying prepared Niobate, b-d) charge-discharge curves of $MnNb_2O_6$, $FeNbO_4$ and $NiNb_2O_6$, respectively.

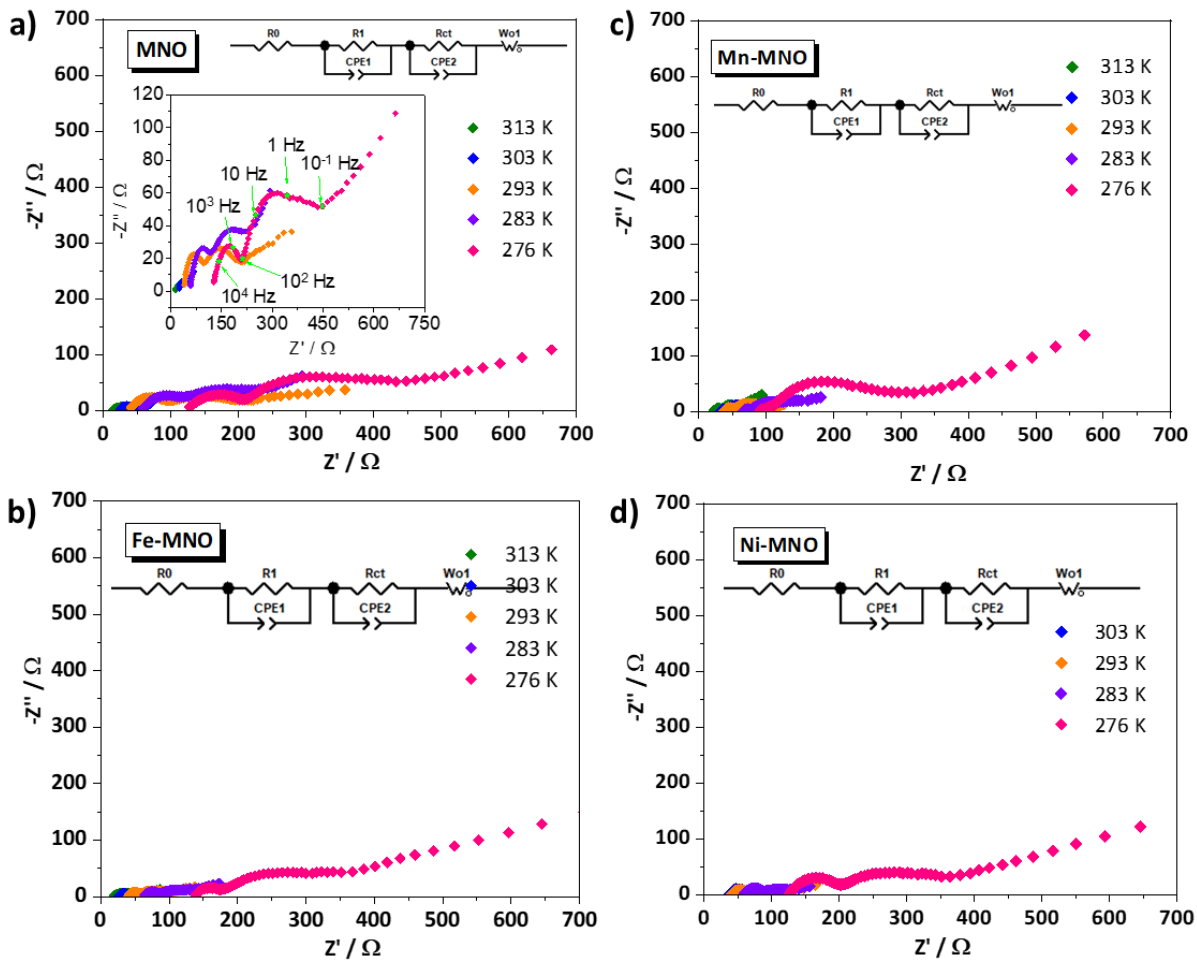


Fig. S10 Electrochemical impedance spectra (EIS) of M-MNO composites in 37 mol $kg^{-1}$ 9LiFSI/1LiTFSI-8$H_2O$/2G4 electrolyte at varying temperatures. a) MNO, b) Fe-MNO, c) Mn-MNO; d) Ni-MNO. (Equivalent circuits are simulated and shown in insertion image).

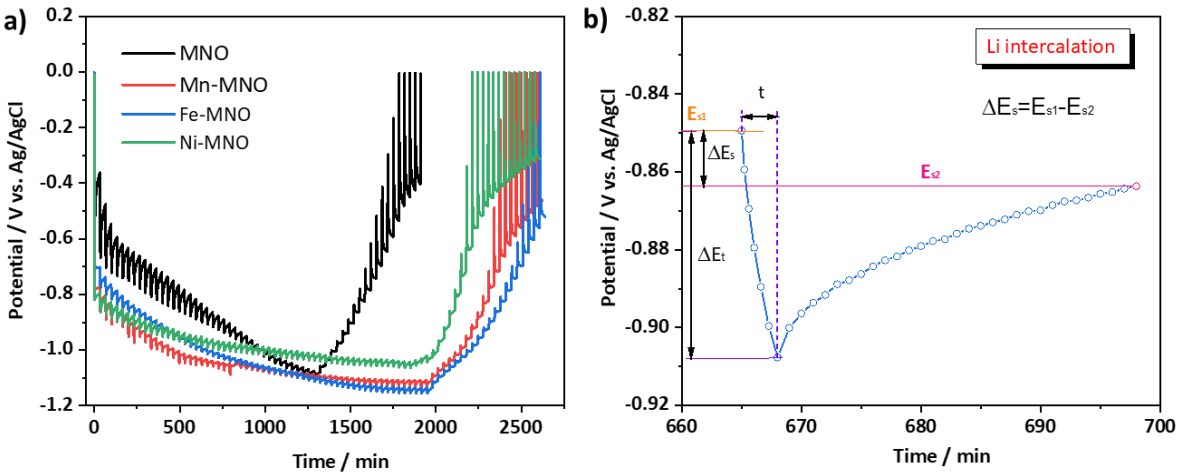


Fig. S11 a) GITT $Li^+$ intercalation-deintercalation curves versus test time of MNO, Mn-MNO, Fe-MNO and Ni-MNO tested in the first cycle with a pulse current of 160 mA $g^{-1}$. b) E versus T curves for a single step in the GITT experiment of MNO.

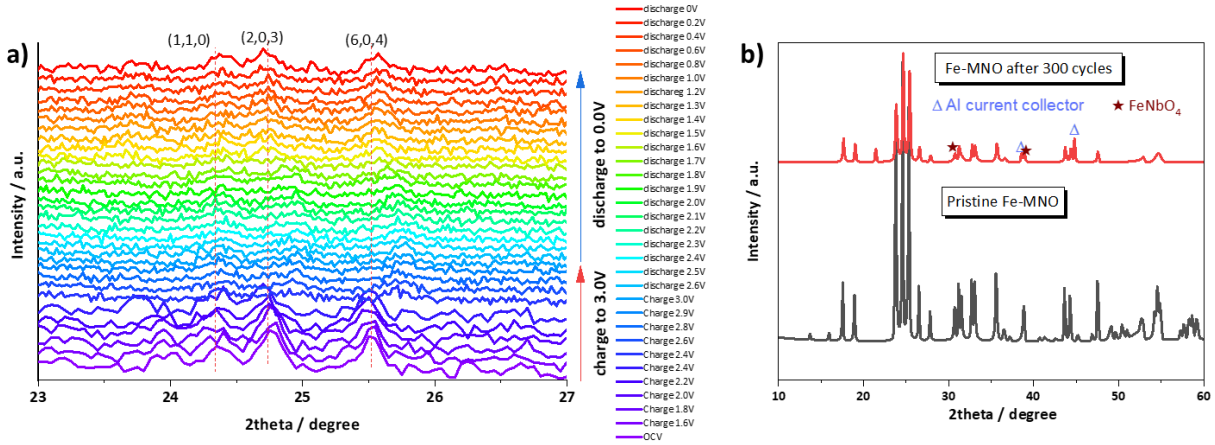


Fig. S12 a) In-situ XRD patterns of Fe-MNO anode in graphite/Fe-MNO dual-ion battery. b) XRD pattern of Fe-MNO after cycling.

The peaks at 23.8°, 24.6° and 25.5° were assigned to $MoNb_{12}O_{33}$ lattice plane of (1,1,0), (2,0,3) and (6,0,4). The XRD patterns of Fe-MNO in charge-discharge process, the peak at 23.8° shows almost no shifting while cell charging. While peaks at 24.6° and 25.4° were shifted to higher angle with charge, and all peaks were recovered to an original as the cell discharge to 0 V, indicating a crystal transformation involved in $Li^+$ insertion into and deintercalation from the Fe-MNO lattice. The XRD pattern of Fe-MNO which was cycled 300 is manifested in Fig. S9b, similar diffraction peaks demonstrated excellent cycle stability.

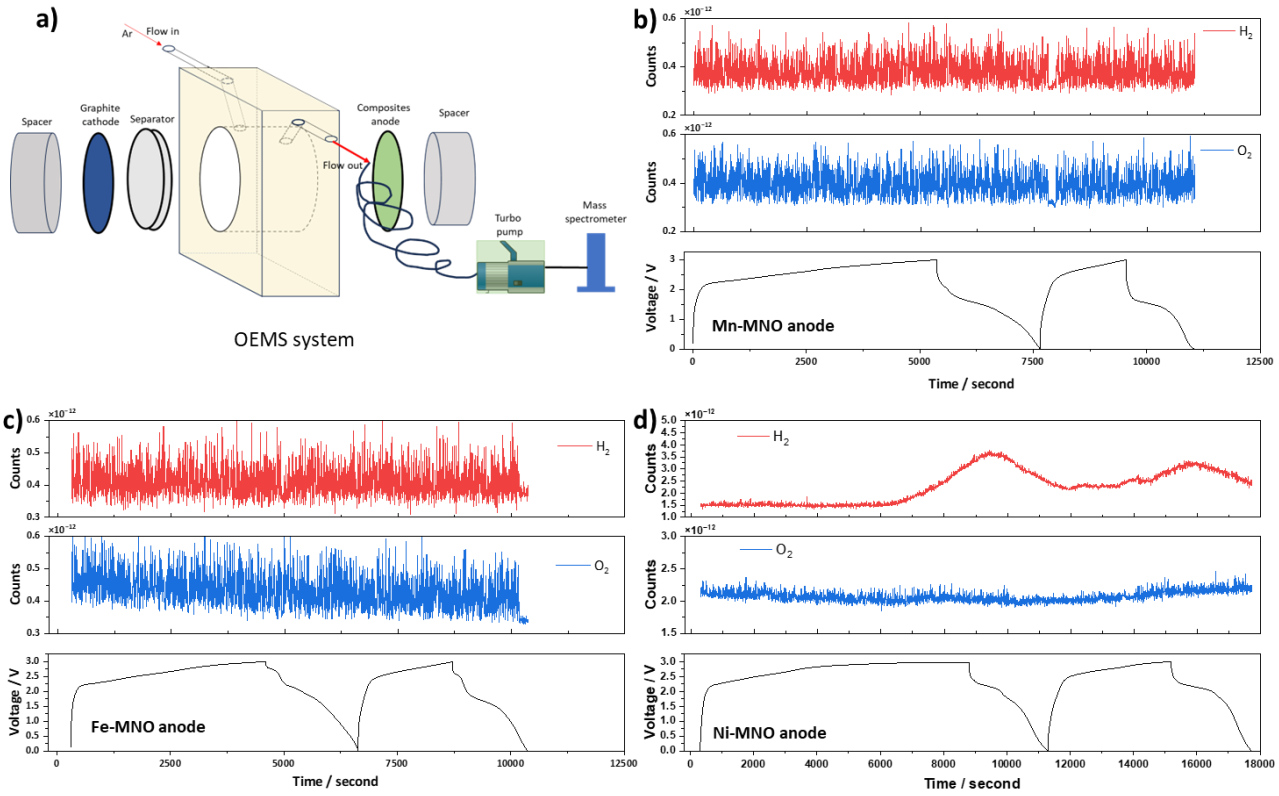


Fig. S13 a) Scheme of employed OEMS set-up system. b) OEMS results at the initial two cycles in a KS6/Mn-MNO full cell. c) OEMS results at the initial two cycles in a KS6/Fe-MNO full cell. d) OEMS results at the initial two cycles in a KS6/Ni-MNO full cell.

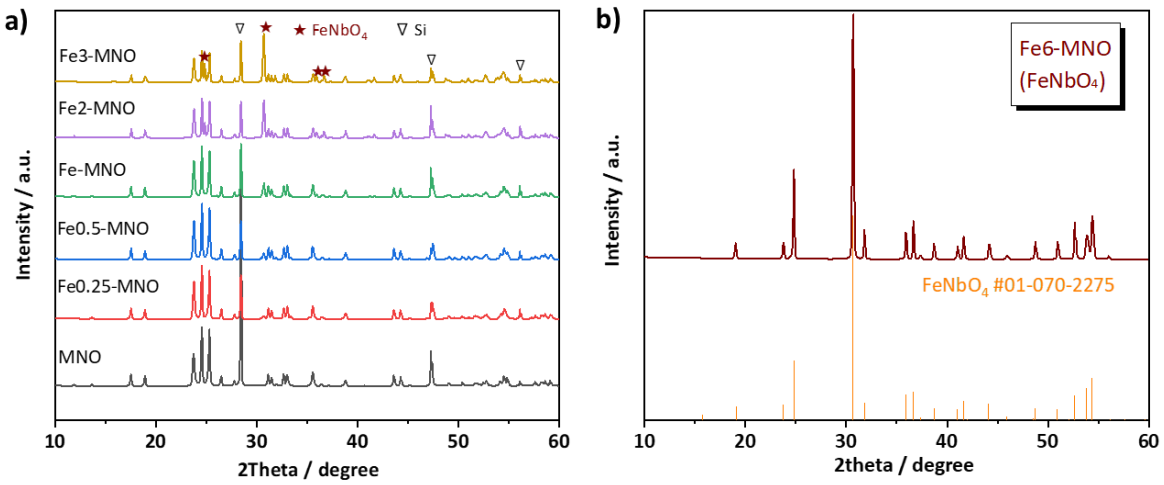


Fig. S14 XRD patterns of synthesized Fe-MNO with varying $FeNbO_4$ contents.

In Fig. S10, XRD patterns of synthesized Fe-MNO composite materials with varying $FeNbO_4$ contents are presented. The numbers after Fe means the molar ratio of Fe/Mo in recipe. With $Fe_2O_3$ usage increased, the intensity of $FeNbO_4$ increased quickly which indicates increased amount of $FeNbO_4$ formation. While the molar ratio of Fe/Mo increases to 6, the product shows only $FeNbO_4$ diffraction peaks. In addition, large amount of $FeNbO_4$ formed in sample also weakened the diffraction peaks of $MoNb_{12}O_{33}$, like Fe3-MNO.

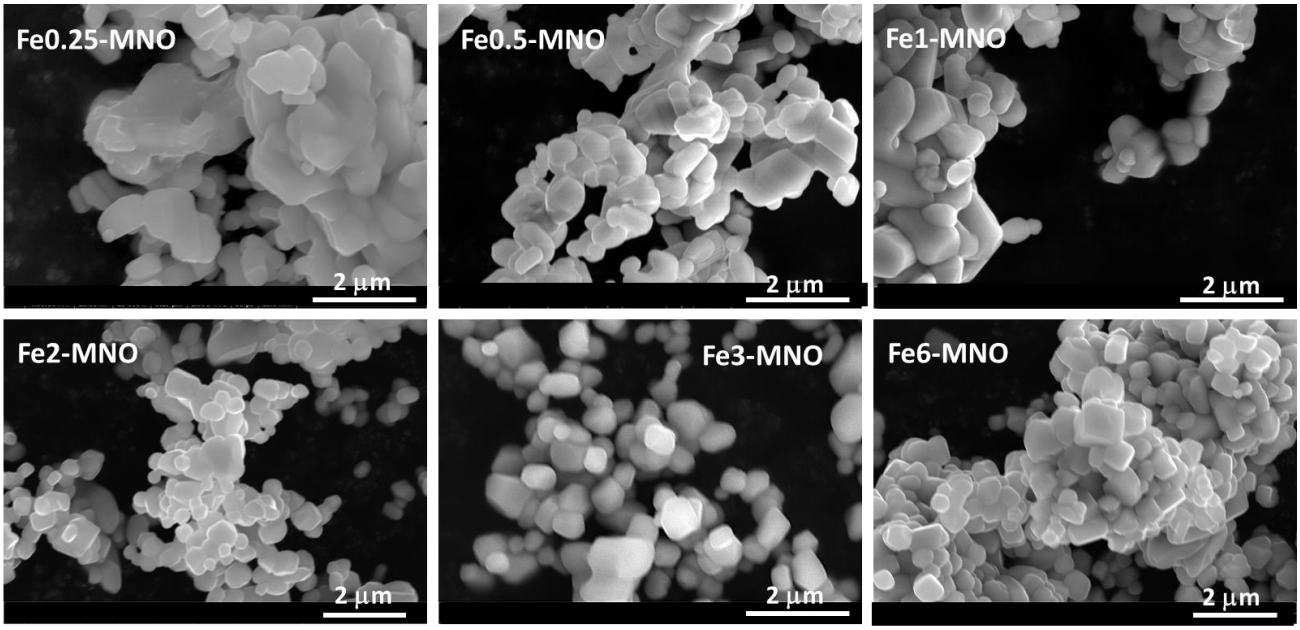


Fig. S15 SEM images of synthesized varied Fe-MNO.

SEM images of synthesized Fe-MNO were shown in Fig. S11. As the Fe content increased, the formed composite particles showed smaller size and approached a cube-like structure.

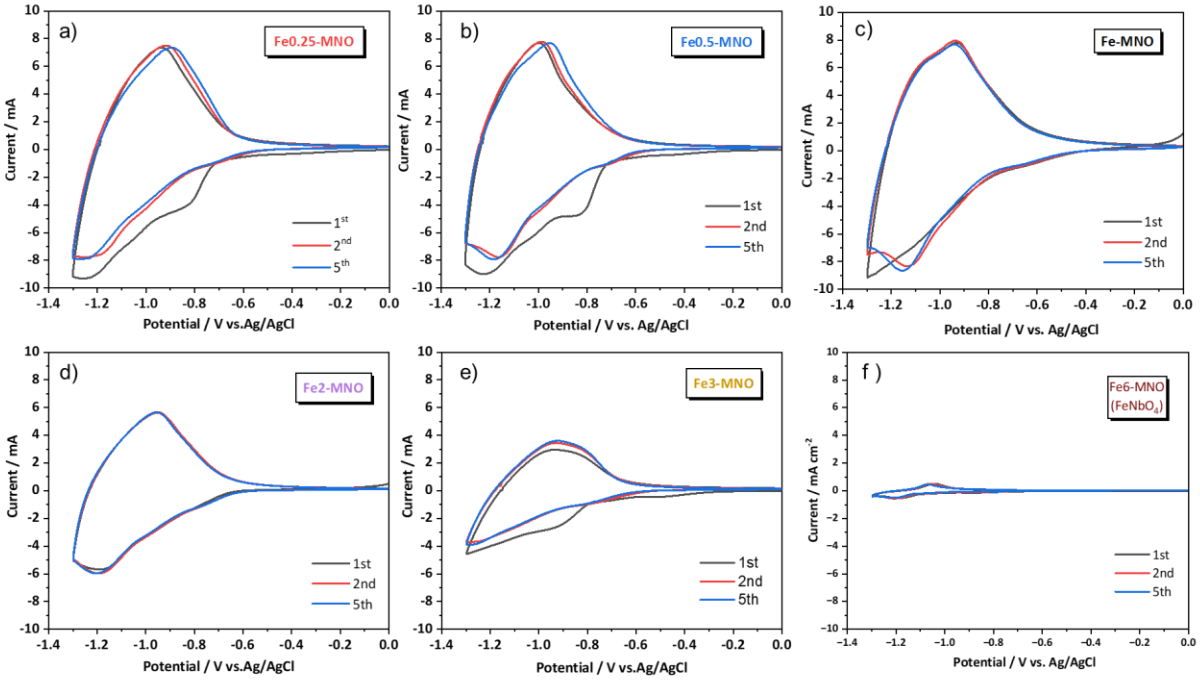


Fig. S16 CV profiles of varied Fe-MNO in 37 mol kg-1 9LiFSI-1LiTFSI/8$H_2O$-2G4 electrolyte. a) Fe0.25-MNO, b) Fe0.5-MNO, c) Fe1-MNO, d) Fe2-MNO, e) Fe3-MNO, f) Fe6-MNO (Potential range: -1.3~0 V; sweep rate: 5 mV $s^{-1}$).

CV measurements were measured for analysis of electrochemical properties of Fe-MNO within potential range of -1.3~0 V vs. Ag/AgCl with a sweep rate of 5 mV $s^{-1}$. For some samples, like Fe0.25-MNO, Fe0.5-MNO and Fe1-MNO, the response current peak of $Li^+$ intercalation shifted gradually to the higher potential with formed $FeNbO_4$ content increasing, indicating that a higher amount of $FeNbO_4$ formation can facilitate $Li^+$ intercalate to the electrode. Synthesized composite of $FeNbO_4$-$MoNb_{12}O_{33}$ have been confirmed by the results of EDX mapping, hence, numbers of grain boundary formed during the crystal growth process between $FeNbO_4$ and $MoNb_{12}O_{33}$ from interaction. These grain boundary enables $Li^+$ intercalation reaction to occur more easily.[8-9] However, with a large amount of $FeNbO_4$ formed, the response current remarkably weakened in case of Fe2-MNO and Fe3-MNO (Fig. S12d and e). In contrast, $FeNbO_4$ (Fe6-MNO sample) shows almost no response current of $Li^+$ intercalation (Fig. S12f). Thus, $FeNbO_4$ seems not to be inactive to $Li^+$ intercalation.

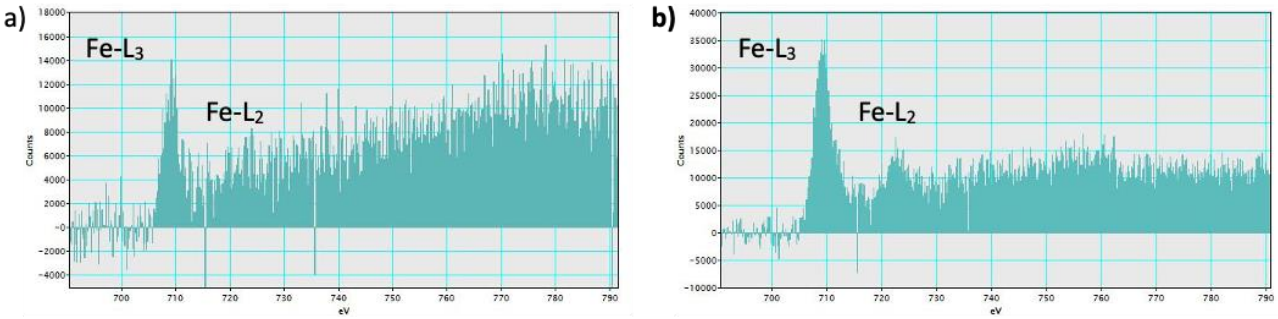


Fig. S17 Electron energy lost spectra (EELS) of Fe-MNO with varying Fe contents. a) Fe0.5-MNO, b) Fe1-MNO.

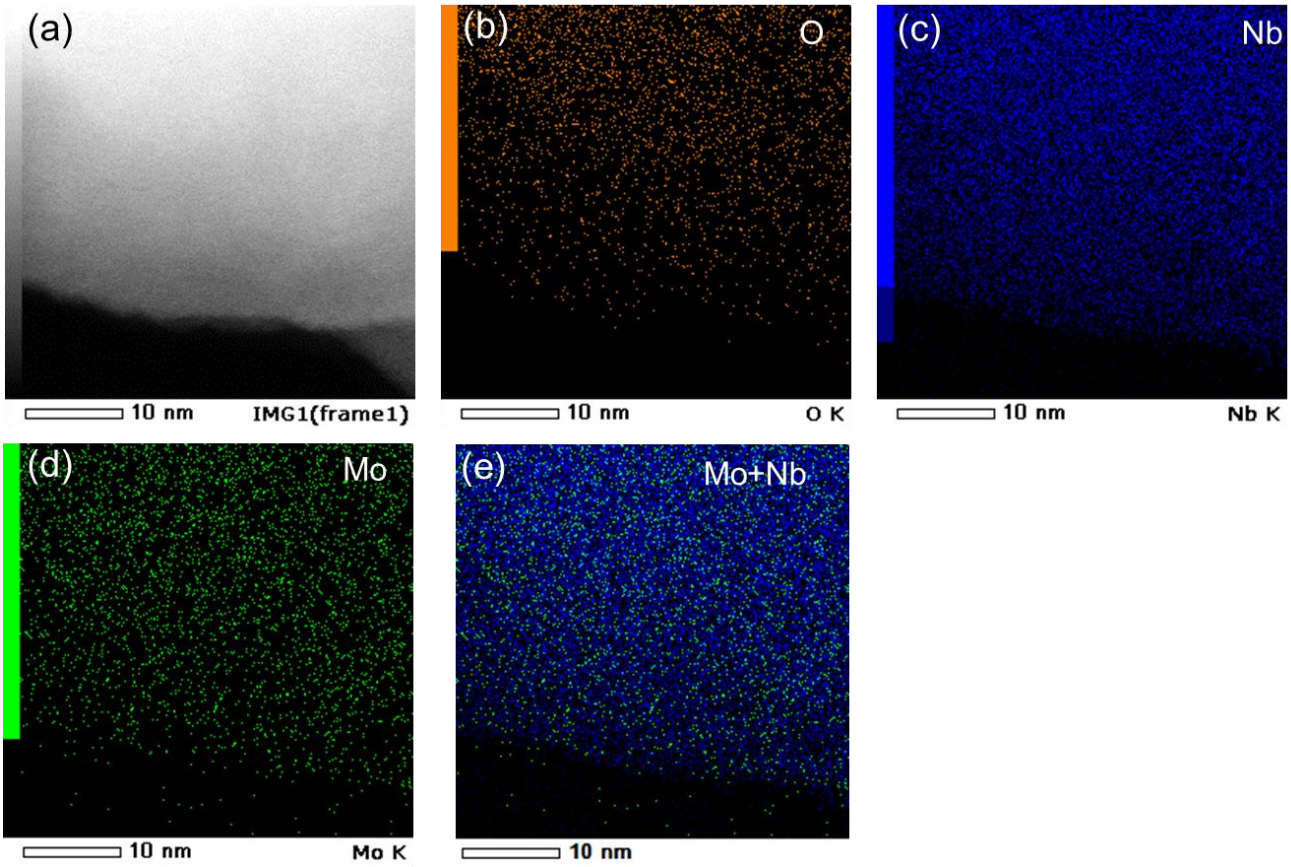


Fig. S18 a) STEM image, b−f) EDX mapping of MNO.

References


[1] D. Yang, H. Li, M. Watanabe, T. Ishihara, *ChemSusChem*, 2022, **16**, 202201805.

[2] X. Li, X. Ou, Y. Tang, *Adv. Energy Mater.* 2020, **10**, 2002567.

[3] L. Xiang, X. Ou, X. Wang, Z. Zhou, X. Li, Y. Tang, *Angew.Chem. Int. Ed. 2020,* **59**, 17924.

[4] X. Wu, Y. Xu, C. Zhang, D. P. Leonard, A. Markir, J. Lu, X. Ji, *J. Ame. Chem. Soc.* 2019, **141**, 6338.

[5] H. Li, T. Kurihara, D. Yang, M. Watanabe, T. Ishihara, *Energy Stor. Mater.* 2021, **38**, 454.

[6] D. Yang, M. Watanabe, A. Takagaki, *J. Electrochem.Soc.* 2022, **169**, 120516.

[7] D. Yang, M. Watanabe, T. Ishihara, *Small Methods* 2023, **7**, 2300249.

[8] S. Zhou, G. Barim, B. J. Morgan, B. C. Melot, R. L. Brutchey, *Chem. Mater.* 2016, **28**, 4492.

[9] P. Schofield, Y. Luo, D. Zhang, W. Zaheer, D. Santos, G. Agbeworvi, J. D. Ponis, J. V. Handy, J. L. Andrews, E. J. Braham, A. R. Balakrishna, S. Banerjee, *ACS Energy Lett.* 2022, **7**, 3286.